

RESEARCH ARTICLE | JUNE 01 2020

Influence of post-deposition annealing on the photoelectrochemical performance of CuBi_2O_4 thin films

Special Collection: **Solar to Fuel**

Marlene Lamers; Michael Sahre; Matthias J. Müller; Daniel Abou-Ras; Roel van de Krol ; Fatwa F. Abdi  

 Check for updates

APL Mater. 8, 061101 (2020)

<https://doi.org/10.1063/5.0003005>



View
Online



Export
Citation

CrossMark

Articles You May Be Interested In

Multi-phase $\text{CuBi}_2\text{O}_4@ \text{CuO} @ \alpha\text{-Bi}_2\text{O}_3$ nanocomposite electrocatalyst for electrochemical water splitting application

AIP Conference Proceedings (July 2019)

False metals, real insulators, and degenerate gapped metals

Appl. Phys. Rev. (November 2020)



yttrium iron garnet, zeolites, nano ribbons, epitaxial crystal growth, cerium oxide polishing powder, surface functionalized nanoparticles, sapphire windows, Nd:YAG, spintronics, silver nanoparticles, MOCVD, rare earth metals, osmium, refractory metals, anodic titanium niobate, perovskite crystals, transparent ceramics, MOFs, AuNPs, ZnS, CdTe

glassy carbon, III-IV semiconductors, barium fluoride, ultra high purity materials, cermet, nanodispersions, MBE grade materials, thin film, OLED lighting, solar energy, sputtering targets, fiber optics, h-BN, deposition slugs, CVD precursors, photovoltaics, metamaterials, borosilicate glass, YBCO superconductors, InGaAs, indium tin oxide, MgF2, rutile, diamond micropowder, optical glass

beamsplitters, fused quartz, gallium lump, copper nanoparticles, organometallics, europium phosphors, photonics, infrared dyes, transparent ceramics, CIGS, cermet, nanodispersions, MBE grade materials, thin film, OLED lighting, solar energy, sputtering targets, fiber optics, h-BN, deposition slugs, CVD precursors, photovoltaics, metamaterials, borosilicate glass, YBCO superconductors, InGaAs, indium tin oxide, MgF2, rutile, diamond micropowder, optical glass



Now Invent.™

www.americanelements.com

© 2001-2022, American Elements LLC, a U.S. Registered Trademark

The Next Generation of Material Science Catalogs

Influence of post-deposition annealing on the photoelectrochemical performance of CuBi_2O_4 thin films

Cite as: APL Mater. 8, 061101 (2020); doi: 10.1063/5.0003005

Submitted: 30 January 2020 • Accepted: 11 May 2020 •

Published Online: 1 June 2020



View Online



Export Citation



CrossMark

Marlene Lamers,^{1,2} Michael Sahre,^{1,a)} Matthias J. Müller,^{1,2} Daniel Abou-Ras,³ Roel van de Krol,^{1,2}  and Fatwa F. Abdi^{1,b)} 

AFFILIATIONS

¹Institute for Solar Fuels, Helmholtz-Zentrum Berlin für Materialien und Energie GmbH, Hahn-Meitner-Platz 1, Berlin 14109, Germany

²Institut für Chemie, Technische Universität Berlin, Straße des 17. Juni 124, 10623 Berlin, Germany

³Department Structure and Dynamics of Energy Materials, Helmholtz-Zentrum Berlin für Materialien und Energie GmbH, Hahn-Meitner-Platz 1, Berlin 14109, Germany

Note: This paper is part of the Special Issue on Solar to Fuel.

^{a)}**Current address:** Department of Chemistry, University of Basel, Klingelbergstrasse 80, Basel CH-4056, Switzerland.

^{b)}**Author to whom correspondence should be addressed:** fatwa.abdi@helmholtz-berlin.de

ABSTRACT

Complex metal oxide semiconductors are promising candidates to be used as photoelectrodes in solar water splitting devices. One particular example is copper bismuth oxide (CuBi_2O_4), which is a p-type semiconductor with an ideal bandgap of 1.6–1.8 eV and suitable band positions. However, the performance has been reported to be limited by photocorrosion and the mismatch between its optical absorption and charge carrier transport properties. It has been shown that the former can be overcome by the deposition of protection layers, while the latter can be addressed by the modification of the bulk properties of the material. Here, we deposited thin films of CuBi_2O_4 using pulsed laser deposition (PLD). This results in high quality films, as evident from the internal quantum efficiency, which is comparable to the best-performing CuBi_2O_4 photoelectrodes. We investigate the bulk modification of the films by exploring post-deposition annealing treatment at various temperatures and oxygen partial pressures. These post-deposition annealing parameters influence the morphology of the films through the formation of aggregated particles/islands with higher crystallinity. The anneal treatment reduces bulk recombination in the film and increases the AM1.5 photocurrent by a factor of more than three. The influence of the high temperature post-deposition annealing treatment on other properties of CuBi_2O_4 (absorption, formation, and suppression of defects) is also discussed. This study underlines the importance of high temperature post-deposition annealing treatment in optimizing the performance of complex metal oxide photoelectrodes.

© 2020 Author(s). All article content, except where otherwise noted, is licensed under a Creative Commons Attribution (CC BY) license (<http://creativecommons.org/licenses/by/4.0/>). <https://doi.org/10.1063/5.0003005>

Copper bismuth oxide (CuBi_2O_4) has recently emerged as an interesting material to be used as a photocathode in solar water splitting devices. It is a p-type semiconductor with a suitable bandgap of 1.6–1.8 eV,^{1–5} corresponding to a theoretical maximum AM1.5 photocurrent of $\sim 20 \text{ mA cm}^{-2}$. The band positions straddle the water reduction and oxidation potentials, and the photocurrent onset potential is relatively high at $\sim 1 \text{ V}$ vs the reversible hydrogen electrode potential (RHE).^{5–9} Like many copper-based oxides, however, it suffers from photocorrosion; Cu^{2+} readily reduces to Cu^+

and Cu under operating conditions.^{5,10,11} This can be mitigated by the deposition of protection layers. For example, the combination of a CdS buffer layer, TiO_2 passivation layer, and Pt catalyst has resulted in an extended stability of CuO and CuBi_2O_4 photocathodes for photoelectrochemical hydrogen production.^{12,13}

Another limitation of the material is the mismatch between its optical absorption and charge carrier transport properties. The charge carrier mobility is in the range of $10^{-3} \text{ cm}^2 \text{ V}^{-1} \text{ s}^{-1}$, and the charge carrier diffusion length is in the order of tens of nm.⁵

On the other hand, the absorption coefficient is modest; a thickness of ~ 300 nm is required to absorb enough photons to generate 10 mA cm^{-2} . To overcome this, external metal dopants (e.g., Ag) and gradient concentration of copper vacancies ($V_{\text{Cu}}^{\prime\prime}$) have been introduced in CuBi_2O_4 photocathodes.^{8,12} As a result, record AM1.5 photocurrents of $\sim 3 \text{ mA cm}^{-2}$ at 0.6 V vs RHE have been reported in the presence of H_2O_2 as an electron scavenger.^{12,14} Unassisted solar water splitting devices with tandem oxide absorbers have also been reported using CuBi_2O_4 as the photocathodes.^{15,16}

Despite the recent progress, the reported photocurrents are still far from the theoretical limit. One important aspect still overlooked is the influence of the specific conditions (e.g., temperature and oxygen partial pressure) during the post-deposition annealing treatment. It has been found for other metal oxides (e.g., Fe_2O_3 or BiVO_4) that the annealing conditions can have a large influence on the photoelectrochemical properties.^{17,18} In the present work, we perform a systematic study to correlate the influence of temperature and oxygen partial pressure during the post-deposition annealing treatment to the photoelectrochemical properties of CuBi_2O_4 thin films prepared by pulsed laser deposition (PLD). PLD-deposited CuBi_2O_4 films have been recently reported to demonstrate superior photoelectrochemical stability.¹⁹ We find that an optimized annealing environment and temperature improve the photocurrent and the absorbed photon-to-current efficiency (APCE) of the CuBi_2O_4 films by a factor of >3 . The true nature of this performance improvement is then revealed through detailed structural and defect investigations of the various films.

The influence of post-deposition annealing treatment on the crystal structure of CuBi_2O_4 thin films was first investigated through x-ray diffraction (XRD) measurements. Details on the sample preparation steps and characterization methods can be found in the [supplementary material](#). The grazing incidence x-ray diffractograms of all CuBi_2O_4 films on fluorine-doped tin oxide (FTO) annealed at different temperatures between 450°C and 650°C in air show a pure tetragonal CuBi_2O_4 phase (space group $P4/nnc$, JCPDS 01-080-0994) (Fig. S2). No traces of phase impurities (e.g., CuO and Bi_2O_3) are detected. The crystallinity of the films increases with higher post-deposition annealing temperature, as evidenced from the decrease in the full width at half maximum (FWHM) of the reflections.^{20,21} Post-annealing in argon ($p\text{O}_2 \sim 1 \times 10^{-4}$ bar) has also been attempted, but this results in phase segregation (Fig. S3). Since phase segregation is undesired in our study, we therefore focus further analysis only on films post-annealed in air and at higher $p\text{O}_2$.

Figure 1(a) shows the AM1.5 photocurrent–voltage curves measured in dark and under illumination for CuBi_2O_4 films annealed in air at temperatures between 450°C (black) and 650°C (red). The electrolyte used was 0.1M potassium phosphate buffer (KP_i, pH ~ 7) with H_2O_2 as an electron scavenger as it has been reported that CuBi_2O_4 is relatively stable in this electrolyte.^{5,9,19} Higher photocurrents are clearly detected with the increase in annealing temperature. This is summarized in Fig. 1(b), where the photocurrents at 0.8 V vs RHE for the various films are plotted as a function of the annealing temperature. The main photocurrent improvement is achieved between 500°C and 550°C ; in this temperature range, an increase in the post-deposition annealing temperature by only 50°C results in a 3-fold enhancement of the photocurrent.

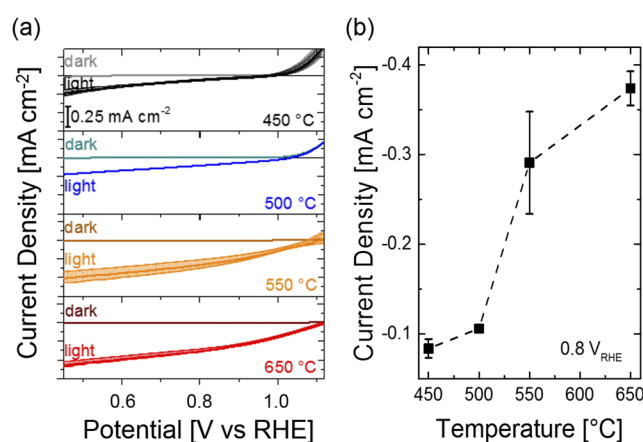


FIG. 1. (a) AM1.5 photocurrent–voltage curves and (b) the photocurrent trend at 0.8 V vs RHE of CuBi_2O_4 films annealed in air at 450°C (black), 500°C (blue), 550°C (orange), and 650°C (red). The electrolyte was a 0.1M potassium phosphate (KP_i) buffer (pH ~ 7) with added 6% H_2O_2 as electron scavengers.

We note that the obtained photocurrents in Fig. 1 are modest compared to the highest photocurrents reported for CuBi_2O_4 . We attribute this to the fact that relatively thin films of only 120 nm were used (see Fig. S4), which limits the amount of absorbed photons. Moreover, we note that no further improvement strategies, such as Ag-doping or gradient homojunction of copper vacancies,^{8,12,14} were used for these films. We will show later that the films nevertheless have comparable APCE with the best-performing CuBi_2O_4 photoelectrodes. Despite the limited thickness, the direction of illumination was found to affect the photocurrent; the AM1.5 photocurrent at 0.6 V vs RHE is $\sim 65\%$ higher under back-side illumination as compared to that under front-side illumination (see Fig. S5). Since more photogenerated electrons are located far from the CuBi_2O_4 -electrolyte interface under back-side illumination (for the 120 nm thickness, the number of absorbed photons within the first 25 nm thickness is $\sim 60\%$ larger than within the last 25 nm; see Fig. S6), and assuming a homogeneous distribution of defects and/or crystalline quality throughout the thickness of the film, the higher photocurrent suggests that electrons are transported more efficiently than holes in CuBi_2O_4 .

The relatively large photocurrents for the films after annealing may be caused by several factors. First, the higher annealing temperature could introduce changes in the surface chemistry of the film, which influences the charge transfer efficiency at the CuBi_2O_4 /electrolyte interface. However, this is unlikely to be the reason since H_2O_2 was used in our photoelectrochemical (PEC) measurements; it has been shown that H_2O_2 acts as a facile electron scavenger for CuBi_2O_4 photocathodes.^{5,16,19}

Another possible explanation for the enhanced photocurrent is an increase in the optical absorption upon high temperature annealing. This would result in a higher generation rate of electron–hole pairs and a concomitant increase in the PEC performance. We therefore measured the absorption and the IPCE (incident photon-to-current efficiency) of the films (see Figs. S7 and S8). The absorbed photon flux ($J_{\text{int,abs}}$) and the collected electron flux ($J_{\text{int,IPCE}}$) in the CuBi_2O_4 films annealed at different temperatures can then be

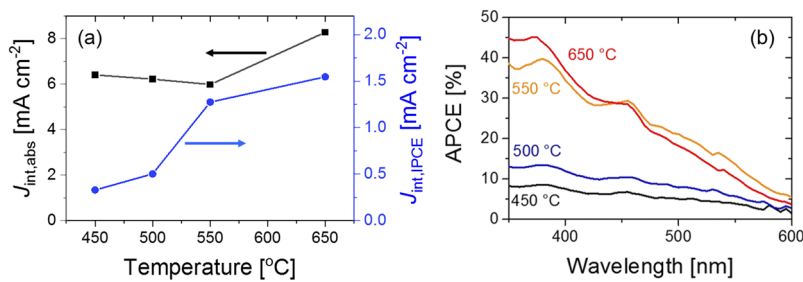


FIG. 2. (a) Total absorbed photon flux expressed in current, $J_{int,abs}$ (black), and total collected electron flux, $J_{int,IPCE}$ (blue), for CuBi_2O_4 films annealed in air at 450 °C, 500 °C, 550 °C, and 650 °C. (b) Absorbed photon-to-current conversion efficiency (APCE) at 0.8 V_{RHE} of CuBi_2O_4 films post-deposition annealed at temperatures of 450 °C (black), 500 °C (blue), 550 °C (orange), and 650 °C (red) in air. The measurements were done under back-side monochromatic illumination, and the electrolyte was 0.1M KPi buffer (pH ~ 7) with added 6% H_2O_2 .

calculated using the following equations:

$$J_{int,abs} = \int [\Phi_{AM1.5}(\lambda) \times A(\lambda) \times e] d\lambda, \quad (1)$$

$$J_{int,IPCE} = \int [\Phi_{AM1.5}(\lambda) \times IPCE(\lambda) \times e] d\lambda. \quad (2)$$

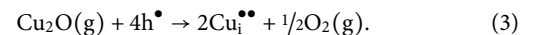
$\Phi_{AM1.5}(\lambda)$ is the flux of incident AM1.5 photons at a specific wavelength, $A(\lambda)$ is the absorption at a specific wavelength, and e is the electronic charge (1.602×10^{-19} C). Figure 2(a) shows the calculated $J_{int,abs}$ and $J_{int,IPCE}$. $J_{int,abs}$ decreases with the increase in annealing temperature between 450 °C and 550 °C. A further increase in annealing temperature to 650 °C results in a 20% increase in $J_{int,abs}$. In contrast, $J_{int,IPCE}$ monotonously increases with the increase in annealing temperature; film annealed at 650 °C shows ~ 5 -fold higher $J_{int,IPCE}$ as compared to that annealed at 450 °C. The discrepancy between $J_{int,abs}$ and $J_{int,IPCE}$ suggests that a change in optical absorption cannot be the main factor behind the improved PEC performance.

Based on the absorption and the IPCE of the films (Figs. S7 and S8), the absorbed photon-to-current conversion efficiency (APCE, also called the *internal* quantum efficiency) values were calculated [Fig. 2(b)]. The APCE of the CuBi_2O_4 films increases with the increase in post-deposition annealing temperature, consistent with the trend in the AM1.5 photocurrent. For the film annealed at 650 °C, the APCE values reach 45% at wavelength < 400 nm. These APCE values are much higher than the electrodeposited $\text{CuBi}_2\text{O}_4/\text{Ag}-\text{CuBi}_2\text{O}_4$ films and comparable with the drop casted CuBi_2O_4 films reported in the literature.^{5,8} This result therefore shows that our film is of relatively good quality; the difference between our modest AM1.5 photocurrent (Fig. 1) and that of the state-of-the-art CuBi_2O_4 is caused by the moderate absorption in our relatively thin (120 nm) films.

Next, we investigate the possibility that the high temperature annealing leads to the formation or suppression of defects in our CuBi_2O_4 films. Although all films show crystalline tetragonal CuBi_2O_4 (see Fig. S2), the defect concentration in the films is typically not large enough to be detected in a normal XRD scan. Therefore, Mott-Schottky measurements were performed in order to determine the effective acceptor density in each film. Since both donor- and acceptor-type defects (e.g., cation and anion vacancies) may be present in our films, we define the effective acceptor density as the difference between the ionized acceptor density (N_A^-) and the ionized donor density (N_D^+). Figure 3(a) shows the effective acceptor density ($N_A^- - N_D^+$) in the CuBi_2O_4 films as a function of the post-deposition annealing temperature in air ($p\text{O}_2 = 0.2$ bar); see Fig. S9

for the Mott-Schottky curves of each film. The effective acceptor density decreases with the increase in post-deposition annealing temperature. This may be caused either by a decrease in N_A^- or an increase in N_D^+ . Sharma *et al.* and Ong *et al.* reported that the dominant acceptor species that defines the p-type nature of CuBi_2O_4 is the copper vacancy ($V_{Cu}^{//}$).^{3,22} Since there is no external Cu source in our experiments, it is not obvious how the concentration of $V_{Cu}^{//}$ can be decreased during our high-temperature annealing treatment. Diffusion of Cu atoms from either the original lattice positions or interstitials would not change the effective acceptor density. Thus, it seems more likely that the decrease in the effective acceptor density is due to an increase in the compensating ionized donor density (N_D^+).

Several defects may act as a donor species in CuBi_2O_4 . One possible defect is copper interstitial (Cu_i^{**}). The formation of Cu_i^{**} can be described by the dissolution of Cu_2O into CuBi_2O_4 ,



Again, since no external Cu source is present during our annealing treatment, this possibility is unlikely to occur and can be ruled out. Alternatively, tin (Sn) could diffuse from the FTO (F-doped SnO_2) substrates into the CuBi_2O_4 films and occupy a Cu lattice site. Sn doping from the FTO can be written as either an electronic or as an

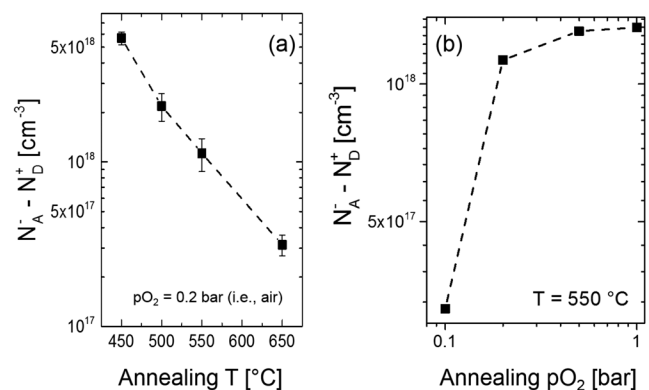
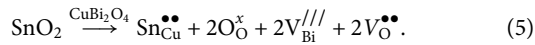
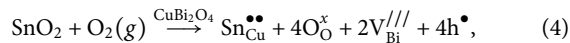


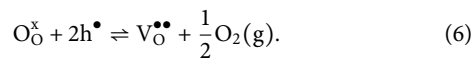
FIG. 3. The effective acceptor density (i.e., the difference between the density of ionized acceptors and ionized donors) of CuBi_2O_4 films post-deposition annealed (a) at different temperatures between 450 °C and 650 °C in air ($p\text{O}_2 = 0.2$ bar) and (b) at 550 °C in different $p\text{O}_2$ (0.1–1 bar).

ionic compensation reaction,



Equation (4) shows that in the case of electronic compensation, the formation of $\text{Sn}_{\text{Cu}}^{\bullet\bullet}$ is accompanied by an increase in the concentration of holes, i.e., an increase in the effective acceptor density. This is clearly inconsistent with the results from the Mott–Schottky measurements. Similarly, in the case of ionic compensation [Eq. (5)], the formation of $\text{Sn}_{\text{Cu}}^{\bullet\bullet}$ does not change the concentration of holes. Again, this does not agree with our experimental observation. Based on this, we conclude that tin diffusion into CuBi_2O_4 films is unlikely to occur.

The donor density (N_{D}^+) may also be increased through the formation of oxygen vacancies based on the following equation:



Since the net change in entropy for reaction (6) is positive ($\Delta S > 0$), the thermodynamic driving force for the creation of oxygen vacancies increases with the increase in annealing temperature. This should lead to a decrease in the electronic conductivity of the material, which is indeed what we observe [Fig. 3(a)]. Equation (6) also predicts a decrease in conductivity with a decrease in oxygen partial pressure. To confirm this, we measured the effective acceptor density of CuBi_2O_4 films as a function of the oxygen partial pressure (p_{O_2}) during the annealing treatment. The results are shown in Fig. 3(b) for a constant annealing temperature of 550 °C. Indeed, the effective acceptor density decreases with the decrease in p_{O_2} , which is in agreement with the expected increase in N_{D}^+ due to the formation of

oxygen vacancies. We note that all these films show a pure tetragonal CuBi_2O_4 phase (see Fig. S10), unlike the one annealed in argon (Fig. S3).

A decrease in the effective acceptor density would increase the depletion or space charge layer width. This would in turn enhance the overall charge separation efficiency and improve the photocurrent. This argument can satisfactorily explain our experimental observation for CuBi_2O_4 films annealed in air at different temperatures: a higher annealing temperature decreases ($N_{\text{A}}^- - N_{\text{D}}^+$) [see Fig. 4(a)] and increases the photocurrent (see Fig. 1). However, the explanation no longer holds for films annealed at different p_{O_2} . The photocurrent reaches a maximum at a p_{O_2} of 0.2 bar (Fig. S11), despite the continuous decrease in ($N_{\text{A}}^- - N_{\text{D}}^+$) with the decrease in p_{O_2} [see Fig. 3(b)]. Figure S12 summarizes the data from both series of samples, and clearly no correlation exists between the effective acceptor density, ($N_{\text{A}}^- - N_{\text{D}}^+$), and the measured photocurrent. Therefore, we can conclude that changes in defect chemistry, i.e., the formation and suppression of oxygen vacancies ($\text{V}_{\text{O}}^{\bullet\bullet}$), are most likely not the main reason for the observed PEC trend.

We now turn our attention to the morphology of the samples. An increase in grain size, for example, can potentially lead to a decrease of charge carrier scattering at the grain boundaries and results in an improved mobility and photocurrent. Figure 4 shows the scanning electron microscopy (SEM) images of our CuBi_2O_4 films. Indeed, the grain size of the films increases with the increase in temperature [Figs. 4(a)–4(d)]. For example, the film annealed at 550 °C [Fig. 4(c)] has more than two and a half times larger grains compared to that annealed at 450 °C [Fig. 4(a)]. A quantitative analysis of the grain sizes reveals average grain sizes of 41 nm, 91 nm, 108 nm, and 210 nm for films annealed at 450 °C, 500 °C, 550 °C, and 650 °C in air, respectively (see Fig. S13 for the statistical histogram). However, annealing the films at different p_{O_2} barely affects the grain size of CuBi_2O_4 (Fig. S14), suggesting that other factors may play a more important role. A closer look into the

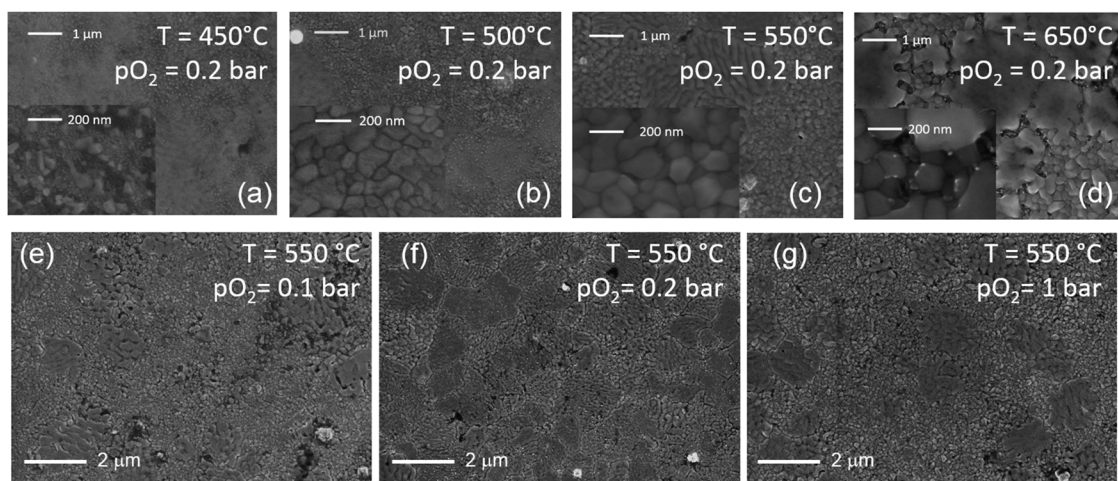


FIG. 4. Scanning electron microscopy (SEM) images of CuBi_2O_4 films [(a)–(d)] annealed in air ($p_{\text{O}_2} = 0.2$ bar) at varying temperatures (450 °C, 500 °C, 550 °C, and 650 °C) and [(e)–(g)] annealed at a temperature of 550 °C with varying p_{O_2} (0.1 bar, 0.2 bar, and 1 bar).

SEM images at smaller magnifications (Fig. 4) reveals the presence of large aggregation of particles, in the following termed “islands” (see Fig. S15 for SEM images within which these are highlighted), at post-deposition annealing temperatures of above 500 °C. The concentration of islands also changes considerably with varying pO_2 : fewer islands were formed after annealing at pO_2 lower or higher than 0.2 bar.

We further quantify the concentration of islands in the films by taking the relative ratio of the sum area of islands to the total area investigated with SEM ($A_{\text{island}}/A_{\text{total}}$). The detected photocurrents for all samples are plotted against the respective concentration of islands in the samples, as shown in Fig. 5(a). A clear correlation is visible: films with higher concentration of islands exhibit higher photocurrents. The photocurrent is also plotted against the reciprocal of the full-width at half-maximum (FWHM) of the dominant 211 reflection in the XRD pattern, i.e., representing the degree of crystallinity, as shown in Fig. 5(b). Again, a clear correlation is observed: films with higher crystallinity feature higher photocurrents. These two correlations [Figs. 5(a) and 5(b)] indicate that the islands may have higher crystallinity than the film matrix. To confirm this, we performed electron backscatter diffraction (EBSD) measurement on the $CuBi_2O_4$ film annealed at 550 °C in air ($pO_2 = 0.2$ bar). Although no dominant orientation exists within the islands, the phase distribution map suggests that the island regions are indeed more crystalline than the rest [see Fig. S16, the area of islands corresponds to the dark smoother regions in panel (a)]. Based on these results, we conclude that the higher crystallinity of the films due to the “island” formation is most likely the main reason for the detected photoelectrochemical performance trend in $CuBi_2O_4$ films.

We note that the difference in the EBSD signal may also be caused by the different roughness between the island and non-island regions, but our atomic force microscopy measurements do not reveal a significant difference in roughness for films with different concentration of islands (see Fig. S17). This also implies that our analysis of the effective acceptor density (Fig. 3) is not affected by

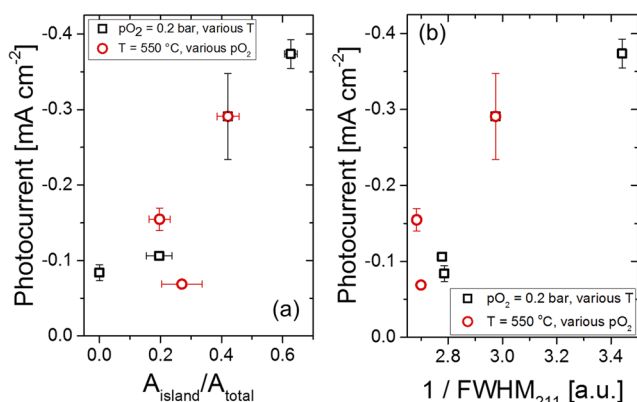


FIG. 5. Photocurrent of various $CuBi_2O_4$ films at 0.8 V vs RHE plotted with respect to (a) relative area of the “island” extracted from SEM images ($A_{\text{island}}/A_{\text{total}}$) and (b) reciprocal of the full-width half-maximum (FWHM) for the (211) XRD reflection peak, i.e., degree of crystallinity. The $CuBi_2O_4$ films were either annealed at a constant temperature of 550 °C but different oxygen partial pressures (pO_2) between 0.1 bar and 1 bar or at a constant pO_2 of 0.2 bar but different temperatures between 450 °C and 650 °C.

the difference in roughness or surface area and therefore still valid (see Fig. S18). Finally, while it is rather straightforward that higher temperatures may have an impact on the formation of islands with higher crystallinity, it is unclear how the oxygen partial pressure during post-annealing may affect the formation of the island morphology. Further investigations beyond the scope of the current work are required in order to reveal the nature of these “islands” and a detailed mechanism of their formation.

In summary, we investigated the influence of a post-deposition anneal at various temperatures and oxygen partial pressures on the PEC properties of pulsed-laser deposited $CuBi_2O_4$ photocathodes. Under optimized conditions, i.e., at a temperature of 650 °C and at $pO_2 = 0.2$ bar, an increase in the AM1.5 photocurrent by a factor of 3 was detected. We showed that this performance improvement is related to the bulk modification of $CuBi_2O_4$ and not to the change in optical absorption or to the formation and suppression of defects in the film. Detailed morphological and crystal structure analyses reveal that this improvement originates from the formation of islands with higher crystallinity and results in increased photocurrent. The formation of islands is shown to depend on the temperature and the oxygen partial pressure during the post-deposition annealing treatment. Overall, the present study highlights the importance and the various roles of post-deposition annealing procedures at elevated temperatures for the modification of the structural, morphological, and photoelectrochemical properties of complex metal oxide photoelectrodes.

See the [supplementary material](#) for (i) detailed experimental methods, (ii) x-ray diffractograms, (iii) profilometry data, (iv) photocurrent–voltage curves under front- and back-side illumination, (v) absorption and IPCE spectra, (vi) photocurrent trends, (vii) Mott–Schottky plots, and (viii) further microstructural analyses of the $CuBi_2O_4$ samples.

We thank Fanxing Xi and Ibbi Ahmet for their assistance in scanning electron microscopy, Klaus Schwarzburg for the help with AFM measurements, and Moritz Kölbach for the support in PLD operation. This work was supported by the German Federal Ministry of Education and Research (BMBF Project Nos. “MeOx-4-H2” and 03SF0478A).

REFERENCES

- T. Arai, Y. Konishi, Y. Iwasaki, H. Sugihara, and K. Sayama, *J. Comb. Chem.* **9**, 574–581 (2007).
- N. T. Hahn, V. C. Holmberg, B. A. Korgel, and C. B. Mullins, *J. Phys. Chem. C* **116**, 6459–6466 (2012).
- G. Sharma, Z. Zhao, P. Sarker, B. A. Nail, J. Wang, M. N. Huda, and F. E. Osterloh, *J. Mater. Chem. A* **4**, 2936–2942 (2016).
- F. F. Abdi and S. P. Berglund, *J. Phys. D: Appl. Phys.* **50**, 193002 (2017).
- S. P. Berglund, F. F. Abdi, P. Bogdanoff, A. Chemseddine, D. Friedrich, and R. van de Krol, *Chem. Mater.* **28**, 4231–4242 (2016).
- K. Sivula and R. van de Krol, *Nat. Rev. Mater.* **1**, 15010 (2016).
- S. P. Berglund, H. C. Lee, P. D. Núñez, A. J. Bard, and C. B. Mullins, *Phys. Chem. Chem. Phys.* **15**, 4554–4565 (2013).
- D. Kang, J. C. Hill, Y. Park, and K.-S. Choi, *Chem. Mater.* **28**, 4331–4340 (2016).
- F. Wang, A. Chemseddine, F. F. Abdi, R. van de Krol, and S. P. Berglund, *J. Mater. Chem. A* **5**, 12838–12847 (2017).
- H. Gerischer, *J. Electroanal. Chem. Interfacial Electrochem.* **82**, 133–143 (1977).
- S. Chen and L.-W. Wang, *Chem. Mater.* **24**, 3659–3666 (2012).

- ¹²F. Wang, W. Septina, A. Chemseddine, F. F. Abdi, D. Friedrich, P. Bogdanoff, R. van de Krol, S. D. Tilley, and S. P. Berglund, *J. Am. Chem. Soc.* **139**, 15094–15103 (2017).
- ¹³W. Septina, R. R. Prabhakar, R. Wick, T. Moehl, and S. D. Tilley, *Chem. Mater.* **29**, 1735–1743 (2017).
- ¹⁴A. Song, P. Plate, A. Chemseddine, F. Wang, F. F. Abdi, M. Wollgarten, R. van de Krol, and S. P. Berglund, *J. Mater. Chem. A* **7**, 9183–9194 (2019).
- ¹⁵J. H. Kim, A. Adishev, J. Kim, Y. S. Kim, S. Cho, and J. S. Lee, *ACS Appl. Energy Mater.* **1**, 6694–6699 (2018).
- ¹⁶J. Li, M. Griep, Y. Choi, and D. Chu, *Chem. Commun.* **54**, 3331–3334 (2018).
- ¹⁷K. Sivula, R. Zboril, F. Le Formal, R. Robert, A. Weidenkaff, J. Tucek, J. Frydrych, and M. Grätzel, *J. Am. Chem. Soc.* **132**, 7436–7444 (2010).
- ¹⁸M. Lamers, S. Fiechter, D. Friedrich, F. F. Abdi, and R. van de Krol, *J. Mater. Chem. A* **6**, 18694–18700 (2018).
- ¹⁹J. Lee, H. Yoon, S. Kim, S. Seo, J. Song, B.-U. Choi, S. Y. Choi, H. Park, S. Ryu, J. Oh, and S. Lee, *Chem. Commun.* **55**, 12447–12450 (2019).
- ²⁰V. Noack and A. Eychmüller, *Chem. Mater.* **14**, 1411–1417 (2002).
- ²¹K. Khojier, H. Savaloni, and Z. Sadeghi, *J. Theor. Appl. Phys.* **8**, 116 (2014).
- ²²E. W. Ong, G. H. Kwei, R. A. Robinson, B. L. Ramakrishna, and R. B. Von Dreele, *Phys. Rev. B* **42**, 4255–4262 (1990).